

A New Model for Elevation Change Estimation in Antarctica From Photon-Counting ICESat-2 Altimetric Data

Rongxing Li¹, Senior Member, IEEE, Youquan He¹, Hongwei Li¹, Yuanyuan Gu, Guojun Li, Gang Qiao¹, Member, IEEE, Huan Xie¹, Senior Member, IEEE, Tong Hao¹, Member, IEEE, and Xiangbin Cui

Abstract—Ice, Cloud, and land Elevation Satellite-2 (ICESat-2) carries a photon-counting laser altimeter with an unprecedented elevation accuracy of 2–4 cm. Since its data availability in 2018, there has been a challenge for the establishment of a new data processing model that can take advantage of this satellite for accurately estimating volumetric changes in Antarctica and associated contribution to global sea level rise (GSLR). We introduce an innovative multitemporal elevation change estimation model (MECEM) that separates precipitation effects from topographic influences to eliminate their correlations and estimates the elevation change rates effectively through a spatiotemporal iterative procedure. The MECEM results are validated by using GNSS in situ observations, snow stakes measurements, and airborne altimetric survey data. The results are also compared with those from ICESat and ESA multimission radar altimetric dataset. It is demonstrated that the model is capable of estimating small thickening of $1.8 \pm 0.1 \text{ cm yr}^{-1}$ in the Vostok subglacial lake region. Using ICESat-2 ATL06 data from 2019 to 2023, the model is proven to be effective in the estimation of elevation change rates in Antarctic basins of different characteristics. Our results show that an increase of $0.103 \pm 0.001 \text{ m yr}^{-1}$ in thickening is found from 2017–2021 to 2019–2023 in Dronning Maud Land. Furthermore, an accelerated thinning by $-0.12 \pm 0.035 \text{ m yr}^{-1}$ is witnessed from 2003–2019 to 2019–2023 in the fast-flowing Pine Island Glacial. With more ICESat-2 data acquired, the developed MECEM model can be applied for estimating the contribution of the entire Antarctic ice sheet (AIS) to GSLR.

Index Terms—Antarctic sensing, climate change, Ice, Cloud, and land Elevation Satellite-2 (ICESat-2), ice mass loss, photon-counting laser altimetry, sea level rise.

I. INTRODUCTION

ICE surface elevation changes are one of the key parameters that measure the amount of ice mass discharged from the

Antarctic ice sheet (AIS) into the Southern Ocean and the associated contribution to the global sea level rise (GSLR) [1], [2]. Thus, the estimation of accurate elevation changes is essential for understanding the ice sheet's response to climate change [3]. As estimated from reconciled solutions from gravimetric, altimetric, and optic and radar imaging satellite observations, from 1992 to 2020, AIS experienced a net mass loss of $2671 \pm 530 \text{ Gt}$, equivalent to $7.4 \pm 1.5 \text{ mm}$ of GSLR [1], [4]. The overall negative mass balance in AIS is attributed to the accelerated ice mass loss in the West Antarctica Ice Sheet (WAIS), at a mass loss rate of $82 \pm 9 \text{ Gt yr}^{-1}$, followed by that in the Antarctic Peninsula Ice Sheet (APIS), at $13 \pm 5 \text{ Gt yr}^{-1}$. The East Antarctica Ice Sheet (EWS) maintained a balanced state of $3 \pm 15 \text{ Gt yr}^{-1}$. However, significant regional ice flow acceleration and mass loss are reported in the Wilkes Land in EAIS since 1960s [2], [5], [6], [7]. Furthermore, with the vast extent of EAIS, elevation uncertainties in altimetric measurements may result in enlarged variations in mass balance estimation [8]. For example, the mass balance estimations of the AIS and regions from the ICESat laser altimetric data of 2003–2008 [9], [10] resulted in mass change rates and trends that are inconsistent with the above reconciled and other mission results [11], [12], [13].

Given a set of altimetric points with measured elevations in a region, the objective is to estimate the volumetric change during the observation period and further to convert the volumetric change to the corresponding ice mass change using additional firn density data and other geophysical observations [14], [15]. Modified from [16], here we establish a general model to quantify factors, such as local topography and precipitation, and simultaneously, to calculate the elevation change rate from the altimetric elevation points. The volumetric change is then calculated through an integration using the change rate. For each altimetric point with elevation Z_{ij} at location (x_{ij}, y_{ij}) , the following general equation can be established:

$$Z_{ij} = \frac{dH}{dt}(t_{ij}) + \sum_{p=0, q=0}^{p \leq p_{\max}, q \leq q_{\max}} (a(p, q)x_{ij}^p y_{ij}^q) + \sum_{r=1}^{\text{end}} \left(c_r \sin\left(\frac{2\pi t_i}{T_r}\right) + d_r \cos\left(\frac{2\pi t_i}{T_r}\right) \right) + \delta_{ij} \quad (1)$$

Manuscript received 11 January 2024; revised 31 March 2024; accepted 27 April 2024. Date of publication 30 April 2024; date of current version 14 May 2024. This work was supported by the Natural Science Foundation of China under Grant 42394131. (Corresponding authors: Youquan He; Gang Qiao.)

Rongxing Li, Youquan He, Hongwei Li, Yuanyuan Gu, Guojun Li, Gang Qiao, Huan Xie, and Tong Hao are with the Center for Spatial Information Science and Sustainable Development Applications, College of Surveying and Geo-informatics, Tongji University, Shanghai 200092, China (e-mail: rli@tongji.edu.cn; 1911211@tongji.edu.cn; lihw@tongji.edu.cn; 2111553@tongji.edu.cn; liguojunlee@tongji.edu.cn; qiaogang@tongji.edu.cn; huanxie@tongji.edu.cn; tonghao@tongji.edu.cn).

Xiangbin Cui is with the Polar Research Institute of China, Shanghai 200092, China (e-mail: cuixiangbin@pric.org.cn).

Digital Object Identifier 10.1109/TGRS.2024.3395522

where $(dH/dt)(t_{ij})$ denotes the elevation change rate at the time t_{ij} (referenced to an initial time t_0) when Z_{ij} is measured. The local topographic surface is considered time invariant during a period and represented as a polynomial with limited orders of p_{\max} and q_{\max} . $a(p, q)$ are the coefficients of the $x_{ij}^p y_{ij}^q$ terms. On the other hand, the modification of the ice surface caused by precipitation is considered time-dependent and described by a series of combined sine and cosine functions. We use c_r and d_r for amplitudes and T_r for cycles (e.g., seasonal and interannual). δ_{ij} is residual attributed to observation errors and truncation effect.

Challenges have been to use a set of realistic satellite altimetric data to solve for all parameters in the ideal model described by (1). Specific difficulties lay in the description of complex terrains in Antarctica, such as snow dunes, crevasses and rifts, and high-slope areas, using altimetric data with a limited point density; similarly, the data may not have a sufficient temporal coverage in austral summer or winter seasons to retrieve the periodical precipitation parameters. For example, due to the limited point density of the ICESat data, a first- or second-order polynomial is used to model the ice surface on the Greenland ice sheet (GIS) from repeat along-track points within each patch [17], [18]. In addition, elevation measurements at crossovers, intersection points between ascending and descending ICESat tracks, are used to estimate elevation changes in GIS and AIS [19], [20]. Finally, an adaptive approach is implemented by [21], where the first-order polynomial is used for terrain modeling.

To model the precipitation effect in GIS using the ICESat data, a combination of sine and cosine functions with one seasonal cycle is applied [17], [18]. An alternative is to use a polynomial to compensate the nonlinearity of this effect [22]. However, with the relatively sparse ICESat elevation points in AIS and errors caused by, e.g., intercampaign bias and others [12], uncertainties of mass balance estimates of East Antarctica are significantly large, even though the same one-cycle precipitation terms are used [1]. This leads to inconsistency between mass change estimates of the entire AIS, resulting in both mass gain and mass loss with significance [1], [11]. A compromise is made to remove the periodical precipitation terms in coastal regions where data are sparser [11], [21]. Therefore, the current state of ICESat-based mass balance estimation in AIS demonstrates that to implement the principle of precision mass balance estimation in AIS using (1), there is an urgent need for new satellite altimetric data beyond ICESat, with higher temporal and spatial coverages for solving the precipitation and terrain parameters. Hence, a new model should be developed to meet the objective.

Ice, Cloud, and land Elevation Satellite-2 (ICESat-2), a successor of ICESat, was launched in September 2018. Data are made available from Cycle 1 and on a rolling basis. In principle, a reliable estimation of AIS mass balance from elevation data of a satellite altimetry mission requires a relatively long period of high-quality data accumulation. Smith et al. [23] used the initial stage data of ICESat-2 (2018–2019) combined with ICESat data (2003–2009) to estimate the elevation change rate of the AIS from 2003 to 2019, using

the crossover points between the two mission tracks. The ICESat-2 mission team released the ATL15 product of elevation change rates (<https://doi.org/10.5067/ATLAS/ATL15.002>, last access: October 25, 2023), which are derived from the ALT06 data by using an extended method of surface elevation reconstruction and change detection (SERAC) [22]. SERAC models the topography from repeated along-track points of an ICESat campaign within a patch by using a third-order polynomial, without precipitation terms; a series of elevation points calculated at the patch center are established from all acquisition campaigns. The elevation change rate is then calculated in an additional one cycle estimation process from the elevation series (product data). This method is successfully applied in the GIS mass balance estimation from the combined ICESat and IceBridge data [15].

In this article, we introduce an innovative “multitemporal elevation change estimation model” (MECEM) that is designed to fully utilize the ICESat-2 superior spatiotemporal ground point coverage patterns and enhanced elevation measurement accuracy in AIS. We propose a three-step approach that estimates periodical precipitation terms and terrain parameters separately, so that their correlations can be eliminated. While the precipitation terms are determined in a larger region to take advantages of ICESat-2’s long-term seasonal measurements, the terrain parameters are computed in smaller along-track windows to model microterrain patterns using densely populated point clouds. The model estimates elevation change rates using observations of all available cycles through an iterative procedure, where the least squares principle is applied to ensure both the estimation accuracy and computational efficiency. Using the ICESat-2 ATL06 data from April 2019 to June 2023 (Cycles 3–19), we implement this new model in four experimental sites with different characteristics, including the largest subglacial lake of Vostok, a drainage basin with positive mass balance in Dronning Maud Land, a drainage basin in the Lambert Glacier–Amery Ice Shelf system (LAS), and the fast-flowing Pine Island Glacier (PIG) region. The modeling results are validated by using airborne altimetric data and in situ observations, such as GNSS and snow stakes. The estimated elevation change rates are compared with longer term estimations from multimission altimetric satellite observations.

II. STUDY AREAS AND DATA

A. Study Areas

We demonstrate the MECEM model and result in four regions with different characteristics, including Vostok subglacial lake region, Basin 5 representing a cumulative region in Dronning Maud Land, Basin 11 with in situ measurements on the Chinese National Antarctic Research Expedition (CHINARE) traverse in EAIS, and Basin 22 containing the fast-flowing PIG in WAIS (see Fig. 1). The drainage basin boundaries are adopted from [24]. Elevation change on the Vostok lake surface is among the lowest in AIS, from 0.3 to 1 mm yr⁻¹ as measured by using GNSS [25] and close to zero as indicated by multiyear altimeter studies [26]. Glaciers in Basin 5 in the Dronning Maud Land region are in a

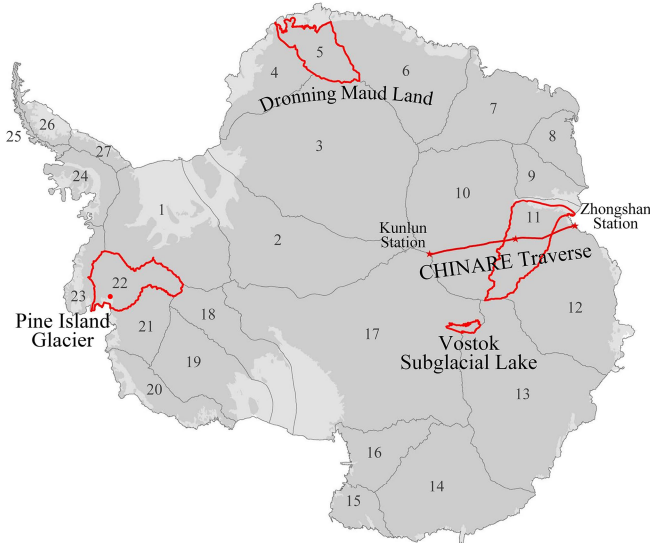


Fig. 1. Study areas (red line and polygons) in AIS include Vostok subglacial lake region, Basin 5 in Dronning Maud Land, Basin 11 along the CHINARE traverse, and Basin 22 in WAIS.

state of balanced or positive mass balance at a thickening rate of $0.12\text{--}0.37\text{ m yr}^{-1}$ [27], [28]. In Basin 11 along the CHINARE traverse, there has been a number of in situ experiments performed for mass balance study [21], [29], including one for ICESat-2 elevation accuracy validation [30]. Finally, Basin 22 contains the PIG where surface thinning reached up to $\sim 1.8\text{ m yr}^{-1}$ near grounding line [26].

B. Data

To reduce the ice mass change estimation uncertainty in cryosphere applications, the ICESat-2 mission aims to increase the elevation measurement accuracy to $2\text{--}4\text{ cm}$ and elevation change rate accuracy to 0.4 cm yr^{-1} by using the new technology of photon-counting laser altimetry [31], [32]. In addition to the increased measurement accuracy, the payload instrument Advanced Topographic Laser Altimeter System (ATLAS) on board ICESat-2 has the advantage, over ICESat that used the full-waveform altimetric technology, of acquiring a large quantity of densely populated elevation points with 3-D coordinates from reflected photons. Specifically, along each ICESat-2 orbit, ATLAS measures the ice surface using three pairs of laser beams, with paired strong and weak beams separated by $\sim 90\text{ m}$ (cross-track); the pairs are separated by $\sim 3.3\text{ km}$ (cross-track) (<https://icesat-2.gsfc.nasa.gov/science/specs>, last access: October 15, 2023). ATLAS emits six beams to the ice surface at the same time and detects returned photons from within each footprint that is $\sim 11\text{ m}$ in diameter on the ground. This measurement process repeats every $\sim 0.7\text{ m}$ along track [31], [33]. ICESat-2 collects data over AIS through 1387 unique orbits over a cycle of 91 days. The mission team released multiple levels of data products since September 2018, among which ATL03 provides elevations of individual returned photons. ATL06 contains land ice surface elevations that are spaced every $\sim 20\text{ m}$ along track, each representing the elevation of a small surface patch estimated collectively from a set of returned photons (ATL03) [34]. The elevation

accuracy of the data products is validated extensively at two different Antarctic sites using coordinated GNSS and other in situ sensor observations [30], [35], [36]. Based on the combined results, ice surface elevations from six beam tracks in ATL06 are accurate to 0.9 cm with a precision of 7.9 cm .

During the initial mission period data from Cycle 1 to Cycle 2 were measured with a dislocation of $1\text{--}2\text{ km}$ away from the designated ground tracks [37], [38]. Thus, data used in this study for implementing and validating the MECEM model include ICESat-2 ATL06 ice surface elevation points over AIS from Cycle 3 to Cycle 19 (from April 2019 to June 2023). To ensure the quality of the data used, we select elevation points by checking the data quality flags, such as ATL06_quality_summary, h_li_sigma, snr_significance, and others.

The brief description and access information for auxiliary data used for validating the ICESat-2 elevations and change rates in the four study sites are given in Table III of Appendices.

III. NEW HIERARCHICAL MULTITEMPORAL ELEVATION CHANGE ESTIMATION MODEL

A. MECEM Framework

ATLAS employs a split-beam design, dividing each laser pulse into six distinct beams and creating a spatiotemporally dense coverage through ICESat-2's ground tracks and revisit cycles [31]. Within a cycle, a region on AIS can be filled by a number of AD-boxes [black boxes in Fig. 2(a)] that are $\sim 20\text{ km}$ in size and formed by ground tracks of an ascending orbit and a descending orbit [see Fig. 2(b)] with a time span ranging from less than 1 day to 91 days. Within each AD-box are four diamond-shaped units (diamond units), where four crossovers are located at each corner, formed by a pair of ascending beams and a pair of descending beams (strong and weak beam pairs). Despite of a lower density distribution, the crossovers contain high-quality direct elevation measurements [20], [23].

We perform an analysis of crossovers of the ICESat-2 ATL06 data in the entire AIS, as well as in the Vostok subglacial lake that is often a calibration and validation test site for satellite altimetry missions (Appendix A). It is demonstrated that the ATL06 crossovers have an unprecedented high point density, in average, one crossover per 2 km cell ($2\text{ km} \times 2\text{ km}$). Elevations at crossovers within each ICESat-2 cycle are of a very high precision because they are measured within a short time span and any influence of time-dependent changes can be minimized. Hence, crossovers obtained in different cycles can be used to capture longer term signals, such as periodical precipitation terms.

Another analysis is performed to investigate the effect of periodical changes, such as precipitation, on the elevation within a limited area (Appendix B). Our results in the Vostok region and three representative AIS basins show that the precipitation effect on the elevation may not vary significantly within a diamond unit and can be modeled by using one set of precipitation terms with two periodical cycles.

To fully utilize the above advantageous spatiotemporal characteristics of the ICESat-2 data, we propose the following

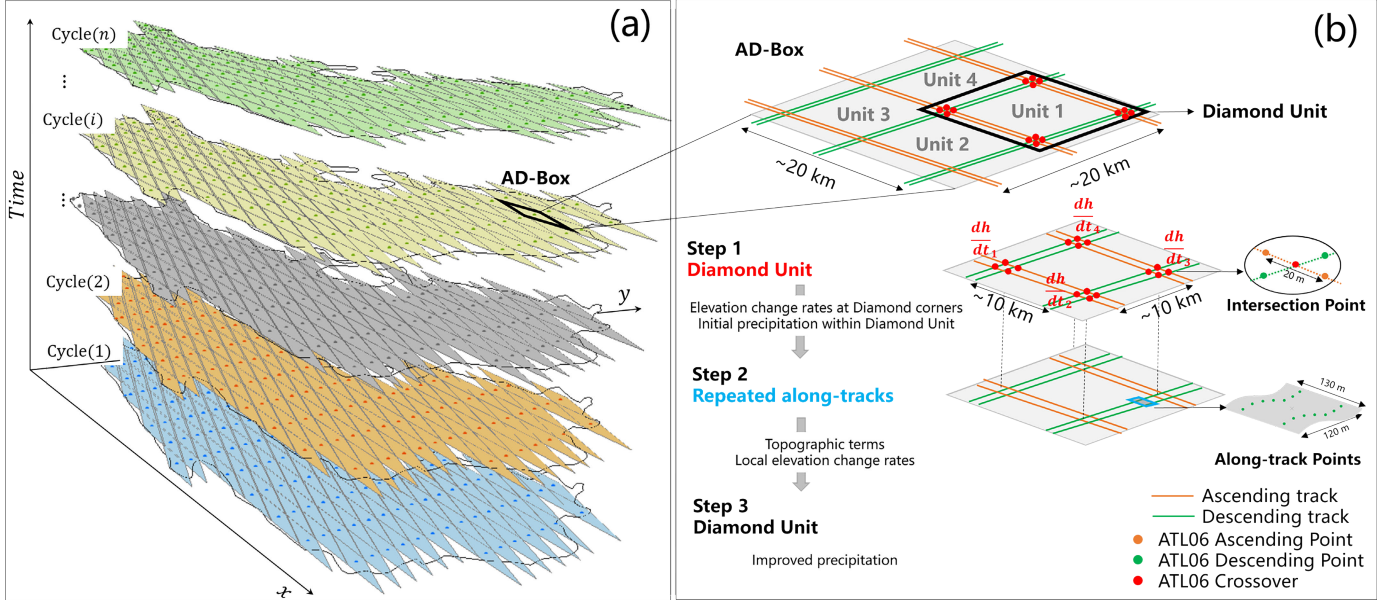


Fig. 2. MECEM framework. (a) Region on AIS filled up by ICESat-2 ATL06 data, temporally by n cycles and spatially by AD-Boxes formed by ascending and descending orbits; and (b) within each AD-box, there are four diamond units that consist of four corners with crossovers and four sides with repeated along-track points. The topographic and precipitation terms are separately solved for in an iterative process to eliminate potential parametric correlations and to increase computational efficiency.

framework of a new hierarchical MECEM. We use three main steps [see Fig. 2(b)] to separate the topographic terms from periodical precipitation terms in the general equation (1), so that potential correlations between these terms can be eliminated. This is particularly important when high-quality altimetric points are less available in the coastal regions [11], [21]. The unknowns, including elevation change rates, topographic parameters, and precipitation parameters, are solved sequentially by using a relatively small amount of well-distributed crossovers of ascending and descending tracks and then a large number of along-track points in an iterative procedure, which is especially computationally effective for handling the ICESat-2 elevation points in the entire AIS.

Step 1: We assume that the precipitation is homogeneous inside each diamond unit of $\sim 10 \text{ km} \times \sim 10 \text{ km}$ [see Fig. 2(b)] and can be modeled by one set of periodical parameters (1) that can be solved by long-term data from Cycle 1 to Cycle n . We use four crossovers at each corner to estimate the initial elevation change and precipitation terms within the entire diamond unit. The topographic terms are not included in this step.

Step 2: Using the elevation change rates at the unit corners and precipitation terms for the entire unit estimated in Step 1 as control, we further use the large number of along-track points on the four sides of the unit [see Fig. 2(b)] to solve for local topographic details. Consequently, we can effectively estimate elevation change rates without the influence of the correlation between the topographic and precipitation terms.

Step 3: Iteratively, based on the known topographic terms computed in step 2, we finally use all available data, crossovers, and along-track points, to refine the precipitation

terms that describe the periodical elevation change in the diamond unit.

The outcome of this three-step iterative procedure represents a robust estimation of elevation change rates from the ICESat-2 data by implementing the principle mathematical model in (1).

B. MECEM Implementation Aspects

The above MECEM framework can be summarized by Fig. 3 for implementation. The input data mainly include ICESat-2 ATL06 ice surface elevation product that contains elevation points, each of which is derived from elevations of photons returned from an ice surface area of 40-m-long along-track. The ATL06 elevation points are spaced every 20-m along-track. These elevation points are preprocessed to establish a hierarchical structure containing AD-boxes, diamond units, corners with crossovers, and sides with along-track points. Then, we use a three-step iterative procedure to compute precipitation and topographic terms. The final results are the elevation change rates and volumetric changes of the region covered by the ICESat-2 data.

Specifically, step 1 is to compute the initial precipitation terms from 16 crossovers at four corners of a diamond unit. Since the ATL06 elevation points are spaced every 20-m along-track, the exact location of a crossover is determined as the intersection between the ascending and descending tracks [see enlarged part of step 1 in Fig. 2(b)] using the algorithm provided by [39]. Then, at each crossover (x_{ij}, y_{ij}) , we have two elevation observations, z_{ij}^A from the ascending track and z_{ij}^D from the descending track, each of which can be applied to establish an observation equation in (1). Their difference

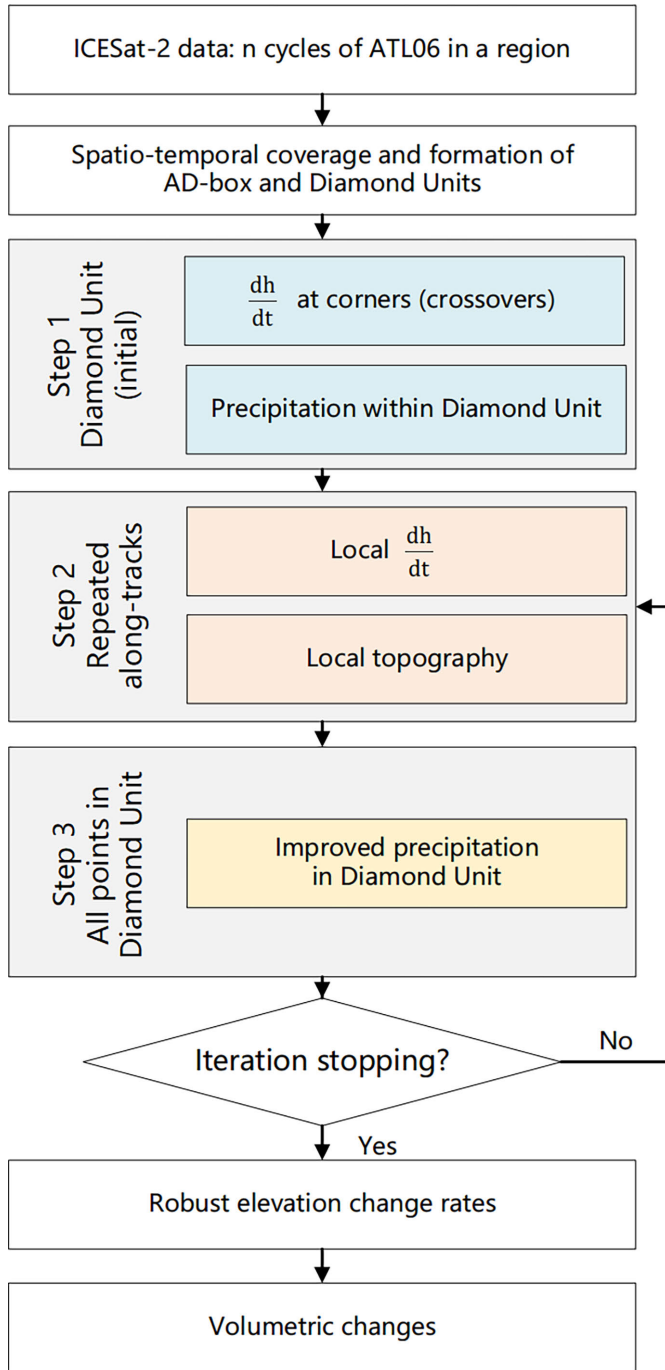


Fig. 3. Implementation diagram of the MECEM model.

makes a new observation equation at each crossover, where only time-dependent elevation change rate and precipitation terms are to be estimated

$$\begin{aligned} \Delta z(t_{ij}^A, t_{ij}^D) &= \frac{dh}{dt}(t_{ij}^D - t_{ij}^A) + \sum_{r=1}^2 \left(c_r \sin\left(\frac{2\pi t_{ij}^D}{T_r}\right) + d_r \cos\left(\frac{2\pi t_{ij}^D}{T_r}\right) \right) \\ &\quad - \sum_{r=1}^2 \left(c_r \sin\left(\frac{2\pi t_{ij}^A}{T_r}\right) + d_r \cos\left(\frac{2\pi t_{ij}^A}{T_r}\right) \right) + \varepsilon_{ij} \end{aligned} \quad (2)$$

where $\Delta z(t_{ij}^A, t_{ij}^D) = z_{ij}^D - z_{ij}^A$. The elevation change rate (dh/dt) is evaluated separately for each corner. We use two sets of periodical parameters, including amplitudes (c_r, d_r) and periodical cycles T_r , with $r = 1$ and 2 . T_1 is set as a fixed cycle of one year and T_2 is treated as an unknown to adjust for any deviation from T_1 . The periodical parameters are used to model the precipitation modification on the topographic surface within the entire diamond unit; thus, they are location independent within the unit. Equation (2) is populated at all 16 crossovers.

In step 2, we use the above initial precipitation terms in the diamond unit to solve for the topographic terms on the four sides of the unit [see Fig. 2(b)]. We open consecutive windows of 120 m (along-track) \times 130 m (cross-track), which contain repeated points along the weak–strong beam track pair with elevation observations z_{ij} at (X_{ij}, Y_{ij}) . Within each window, we model the ice surface topography by using a third-order polynomial

$$\begin{aligned} Z_{ij} - \sum_{r=1}^2 \left(c_r \sin\left(\frac{2\pi t_{ij}}{T_r}\right) + d_r \cos\left(\frac{2\pi t_{ij}}{T_r}\right) \right) &= \frac{dh}{dt}(t_{ij} - t_0) + a_0 + a_1 \left(\frac{X_{ij} - X_0}{l_0}\right) \\ &\quad + a_2 \left(\frac{Y_{ij} - Y_0}{l_0}\right) + a_3 \left(\frac{X_{ij} - X_0}{l_0}\right)^2 + a_4 \left(\frac{Y_{ij} - Y_0}{l_0}\right)^2 \\ &\quad + a_5 \left(\frac{X_{ij} - X_0}{l_0}\right) \left(\frac{Y_{ij} - Y_0}{l_0}\right) \\ &\quad + a_6 \left(\frac{X_{ij} - X_0}{l_0}\right)^3 + a_7 \left(\frac{X_{ij} - X_0}{l_0}\right)^2 \left(\frac{Y_{ij} - Y_0}{l_0}\right) \\ &\quad + a_8 \left(\frac{X_{ij} - X_0}{l_0}\right) \left(\frac{Y_{ij} - Y_0}{l_0}\right)^2 \\ &\quad + a_9 \left(\frac{Y_{ij} - Y_0}{l_0}\right)^3 + \delta_{ij} \end{aligned} \quad (3)$$

where a_0 represents the elevation at the window center (X_0, Y_0) . (a_1, a_2, \dots, a_9) are the topographical polynomial coefficients. l_0 is a normalization factor that may be, for example, chosen as half of the window dimension. (dh/dt) is the unknown elevation change rate. All the along-track points in the window observed during the period from Cycle 1 to Cycle n are used to solve for (dh/dt) and (a_0, a_2, \dots, a_9) .

Consequently, in step 3, we treat the topographic terms and elevation change rate obtained from Step 2 as known. We refine the precipitation terms using all along-track points in the diamond unit

$$\begin{aligned} Z_{ij} - a_0 - a_1 \left(\frac{X_{ij} - X_0}{l_0}\right) - a_2 \left(\frac{Y_{ij} - Y_0}{l_0}\right) &- a_3 \left(\frac{X_{ij} - X_0}{l_0}\right)^2 - a_4 \left(\frac{Y_{ij} - Y_0}{l_0}\right)^2 \\ &- a_5 \left(\frac{X_{ij} - X_0}{l_0}\right) \left(\frac{Y_{ij} - Y_0}{l_0}\right) - a_6 \left(\frac{X_{ij} - X_0}{l_0}\right)^3 \\ &- a_7 \left(\frac{X_{ij} - X_0}{l_0}\right)^2 \left(\frac{Y_{ij} - Y_0}{l_0}\right) \end{aligned}$$

$$\begin{aligned}
& -a_8 \left(\frac{X_{ij} - X_0}{l_0} \right) \left(\frac{Y_{ij} - Y_0}{l_0} \right)^2 - a_9 \left(\frac{Y_{ij} - Y_0}{l_0} \right)^3 \\
& - \frac{dh}{dt} (t_i - t_0) \\
& = \sum_{r=1}^2 \left(c_r' \sin \left(\frac{2\pi t_i}{T_r'} \right) + d_r' \cos \left(\frac{2\pi t_i}{T_r'} \right) \right) + \delta_i. \quad (4)
\end{aligned}$$

$(c'_1, d'_1, c'_2, d'_2, T'_2)$ are the improved precipitation parameters in the diamond unit. Uncertainties of the estimated unknowns in (3) and (4) can be computed using the equations in Appendix C.

This three-step computational algorithm is implemented as an iterative procedure. It terminates when the difference between the estimated elevation change rates in the last two iterations is less than a threshold (0.001 cm yr^{-1}) or a maximum number of iterations (15) is reached. These threshold values are determined based on our experiments in different regions of Antarctica. Otherwise, it repeats steps 2 and 3. The final results contain the elevation change rate and local topography in each window and periodical precipitation terms in the diamond unit.

Once this iterative procedure is executed in all four diamond units of an AD-box, we have a set of discrete elevation change rates. We further perform a semiautomatic process to eliminate outliers using the 3σ (standard deviation) rule and MAD metric [18]. At the basin level that is filled with the estimated elevation change rates in all AD-boxes, we generate a grid with a spacing of 5 km in the Antarctic Universal Polar Stereographic (UPS) system by using the weighted sum of elevation change rates in a neighborhood [40], [41]. Consequently, the volume change during the period can be computed through an integral of the change rates in the region where a Lambert azimuthal-equal area projection is used [42], [43].

In each step of the above interactive procedure, the unknowns are estimated using a least-squares (LS) adjustment [44], [45]. Given observation errors of the elevation measurements provided in the input data of ATL06, we compute the errors of the estimated unknowns through an error propagation using the covariance matrices obtained in the LS process. Thus, for each elevation change rate (dh/dt), we have a variance $\sigma_{(dh/dt)}$. Furthermore, in each grid, the uncertainty of the averaged change rate, $\sigma_{(dh/dt)_{\text{Grid}}}$, is obtained through an error propagation from all $\sigma_{(dh/dt)}$ involved.

Hence, within a region or basin with an area A , the equation for estimating uncertainty of the average elevation change rate is derived based the corresponding mass change rate uncertainty [39]

$$\sigma_{\frac{dh}{dt} \text{ Region}} = \frac{1}{A} \sum_{\text{Grid}=1}^{\text{Allgrids}} A_{\text{Grid}} \sigma_{\frac{dh}{dt} \text{ Grid}} \quad (5)$$

where A_{Grid} represents the area of a grid cell.

IV. RESULTS

A. Vostok Subglacial Lake

The Vostok subglacial lake region, located in central East Antarctica (see Fig. 1), is often chosen as a test site for

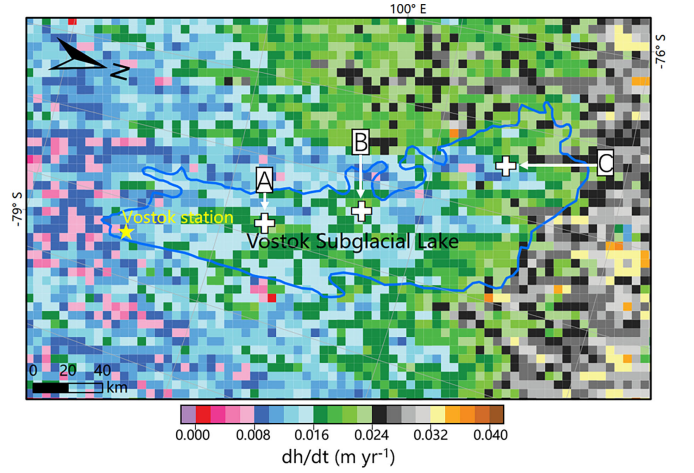


Fig. 4. Estimated ICESat-2 surface elevation change rates in the Vostok subglacial lake region from April 2019 to September 2022. Blue line indicates lake boundary from [48]. Grid spacing is 5 km. Windows A–C (white crosses) are opened to examine precipitation terms. In situ measurements at Vostok Station (star) are used to validate the ICESat-2 elevation change rates.

altimetric mission validation because of its ice surface stability, characterized by low accumulation rates and minimum ice flow velocity. The relatively flat lake surface can also minimize the impact of surface slopes on the altimeter measurement accuracy. The iterative process of the MECEM model in this region generally stops, in average, after ~ 8 iterations. We have a 5-km grid of elevation change rates during 2019–2023 in the $\sim 360 \text{ km} \times \sim 220 \text{ km}$ Vostok region (see Fig. 4).

Vostok Station (star in Fig. 4) was surveyed by using precision GNSS in situ measurements from 2001 to 2013 [25], resulting in a GNSS elevation change rate of $0.1 \pm 0.5 \text{ cm yr}^{-1}$. From the map in Fig. 4, we calculate an MECEM elevation change rate of $1.1 \pm 0.1 \text{ cm yr}^{-1}$ as the average within a 3×3 window centered at Vostok Station. The difference of $1.0 \pm 0.5 \text{ cm yr}^{-1}$ through this direct GNSS–ICESat-2 comparison shows a high accuracy of our estimated elevation change rates, considering that ICESat-2 has an elevation accuracy of 2–4 cm [30], [35], [36], and surface variations may have occurred over the ~ 6 years between the two sets of measurements.

In the entire region, the elevation change rate ranges from ~ 0 to $\sim 3.8 \text{ cm yr}^{-1}$, with an average rate of $1.8 \pm 0.1 \text{ cm yr}^{-1}$ and an increase trend from south to north (see Fig. 4). The majority of the lake area (south part) has a very low elevation change rate of $\sim 1.5 \text{ cm yr}^{-1}$. The elevation change rates in the northern part of the lake area reach up to $\sim 3 \text{ cm yr}^{-1}$, attributing to the region's perennial katabatic wind regime [47] that may have built snow accumulation on the relatively elevated terrain along the periphery of the lake.

We open three windows (diamond units), Windows A–C in Fig. 4, which are relatively evenly distributed in the lake region, to examine the effectiveness of the precipitation term modeling on improving the elevation change rate estimation. As shown in Fig. 5, the periodical curves in all three windows exhibit a seasonal cycle in the region that is represented by the fixed cycle of one year T_1 and adjusted locally by the unknown cycle T_2 separately in three windows; the average

TABLE I
ELEVATION CHANGE RATES, UNCERTAINTY, AND PERIODICAL
CURVE FITTING ERROR IN THREE WINDOWS

Window	$\frac{dh}{dt}$ (m yr ⁻¹)	$\sigma_{\frac{dh}{dt}}$ (m yr ⁻¹)	Curve fitting error (m)
A	0.023	0.001	0.035
B	0.015	0.001	0.032
C	0.013	0.001	0.027

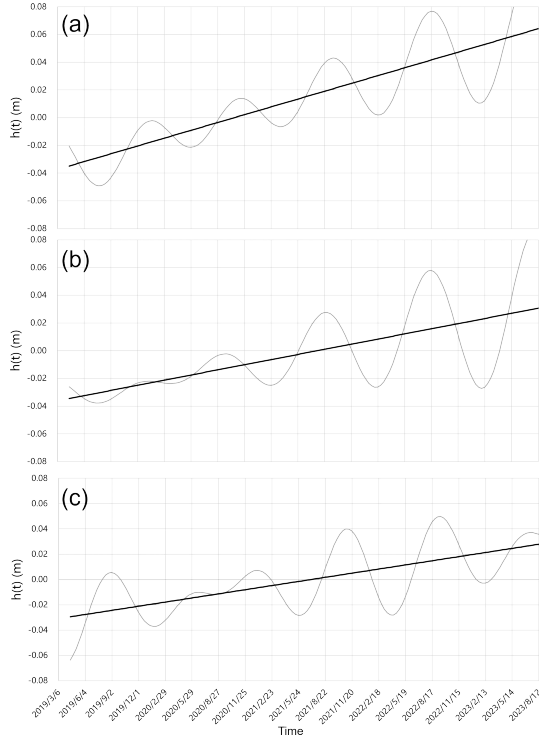


Fig. 5. Periodical terms (gray curves) from precipitation modeling and estimated elevation change rates (black lines) in Windows A–C in the Vostok region (see Fig. 4), as shown in (a)–(c), respectively.

estimated amplitude is ~ 3.8 cm. The resulting curve fitting error ranges from ~ 2.7 to ~ 3.5 cm (see Table I). Since most of precipitation effects is removed in the model, the elevation change rates (black lines in Fig. 5, Table I) in the three windows can be estimated at a mm level, which are given by the model using the covariance propagation.

B. Basin 5 in Dronning Maud Land

The estimated results by the MECEM model show a range from ~ -0.15 m yr⁻¹ to ~ 0.6 m yr⁻¹ in Basin 5 [see Fig. 6(a)], with a broad pattern of ice sheet thickening and the maximum near grounding line of the Fimbul Ice Shelf. The majority of the high inland region shows a low rate of less than ~ 0.08 m yr⁻¹. The average thickening rate is ~ 0.1 m yr⁻¹ in the basin, which is in line with the recent trend of positive mass balance in Dronning Maud Land [5], [23], [49].

We compare the MECEM result from 2019 to 2023 with that from the ESA multimission radar altimetric dataset during 2017–2021 [52]. We compute a difference map between the two datasets (MECEM minus ESA dataset), both of which have a grid spacing of 5 km. In a difficult coast and

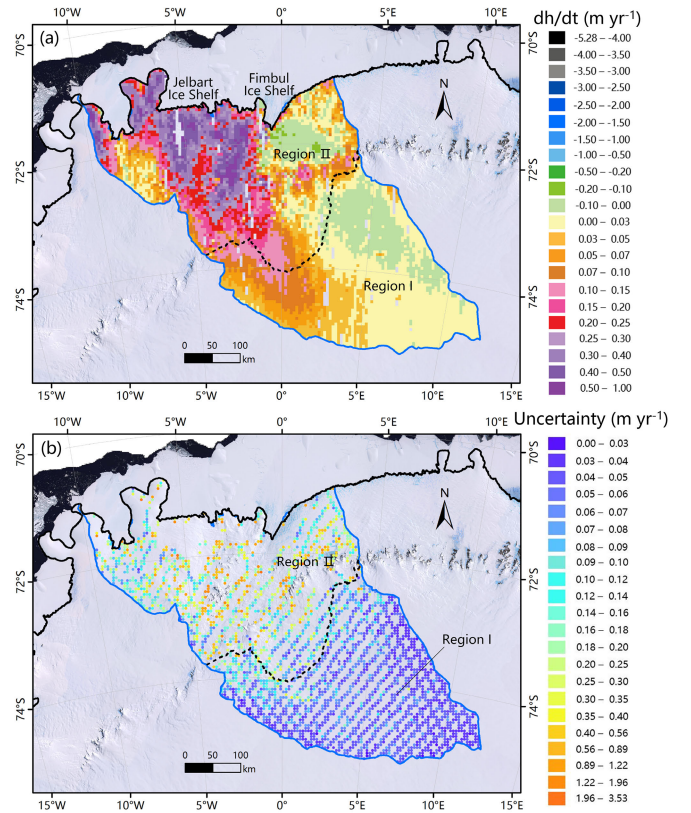


Fig. 6. (a) Estimated ICESat-2 surface elevation change rates in Basin 5. (b) Uncertainty of elevation change rates from ESA multimission radar altimetric dataset for comparison. Regions I and II are separated by an elevation contour of 2600 m (black dashed line). Grid spacing is 5 km in both datasets. Blue line indicates basin boundary [24]. Black line illustrates grounding line [50]. Background is the Landsat image mosaic of Antarctica (LIMA) [51].

fast-flowing region (Amundsen sector), the uncertainty of the ESA dataset change rates reaches 0.52 m yr⁻¹ [53]. However, there are a large number of estimates in the coastal areas with uncertainties greater than 0.5 m [see Fig. 6(b)], attributing to influence factors, such as high terrain slopes, insufficient measurement points, and others [53], [54]. Thus, we separate the basin into Regions I and II using an elevation contour of 2600 m. The comparison between the two datasets is only performed in Region I, the upper inland region, where the average difference is 0.06 ± 0.065 m yr⁻¹. This demonstrates a consistency between the elevation change rates estimated from the ICESat-2 (MECEM) and the ESA dataset in Basin 5.

C. Basin 11 and the CHINARE Traverse

The elevation change rates estimated in Basin 11 (see Fig. 7) show an overall thickening in this eastern tributary region of the Amery Ice Shelf, with an average rate of ~ 0.043 m yr⁻¹. Along the section of the CHINARE traverse that cuts through the basin, the average rate is relatively low, at ~ 0.042 m yr⁻¹. There is a west-ward increasing trend of thickening from the inland interior to the Amery Ice Shelf, ranging from ~ 0.021 to ~ 0.115 m yr⁻¹. The overall low rate and the increasing trend in this region coincide with its descending terrain and katabatic wind effect, which transports surface snow from this side of the ice shelf to the other side [55], [56], [57].

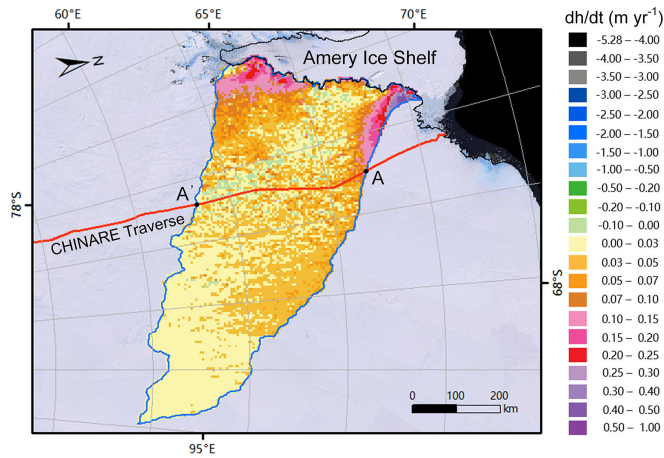


Fig. 7. Estimated ICESat-2 surface elevation change rates in Basin 11. Grid spacing is 5 km. Blue line indicates basin boundary [24]. Black line illustrates grounding line [50]. Background is Landsat image mosaic of Antarctica (LIMA) [51].

In situ surface snow measurements are made along the CHINARE traverse from the Zhongshan Station in the coast to the Kunlun Station at Dome A (see Fig. 1). The traverse section within Basin 11 (AA' in Fig. 7) contains 192 stakes that are spaced every ~ 2 km. The average stake-derived surface mass balance of the upstream region of Profile AA' is 13.8 ± 0.1 Gt yr $^{-1}$ during 1997–2009. Based on in situ GNSS velocity measurements along the profile and other auxiliary data, the ice flux across Profile AA' is estimated as -9.7 ± 0.9 Gt yr $^{-1}$ in the same period [29]. Thus, we obtain the overall mass balance of the upstream region, 4.1 ± 0.9 Gt yr $^{-1}$ during 1997–2009, by subtracting the flux from the surface mass balance.

Furthermore, we convert the estimated ICESat-2 elevation change rate to the mass change rate and to compare with the above in situ observation-based result. First, we make corrections for firn air content (FAC), elastic, and glacier isostatic adjustment (GIA) [23] on the ICESat-2 elevation change rates. Then, we calculate the volumetric change rate from the corrected elevation change rates at all grid cells in the upstream region of the profile AA'. Thus, the ICESat-2 mass balance in the region is calculated as 1.6 ± 0.1 Gt yr $^{-1}$ during 2019–2023 by converting the volume change rate using a firn density of 381 kg m^{-3} [21]. Consequently, the difference between the ICESat-2 and in situ observation-based mass balance results is computed as -2.5 ± 0.9 Gt yr $^{-1}$ and is considered to be very small, considering the uncertainties and time period difference (1997–2009 versus 2019–2023).

D. Basin 22 and Pine Island Glacier

Elevation change during 2019–2023 in Basin 22 varies significantly from a thickening rate of $\sim 0.023 \text{ m yr}^{-1}$ in the southern high inland region to a thinning rate of $\sim -0.566 \text{ m yr}^{-1}$ in the northern part containing PIG [see Fig. 8(a)], which is one of the glaciers with the highest ice mass loss in Antarctica. The average elevation change rate of the entire basin is $-0.384 \pm 0.004 \text{ m yr}^{-1}$. Within PIG, the grounded ice sheet experienced drastic thinning. Especially, there is an

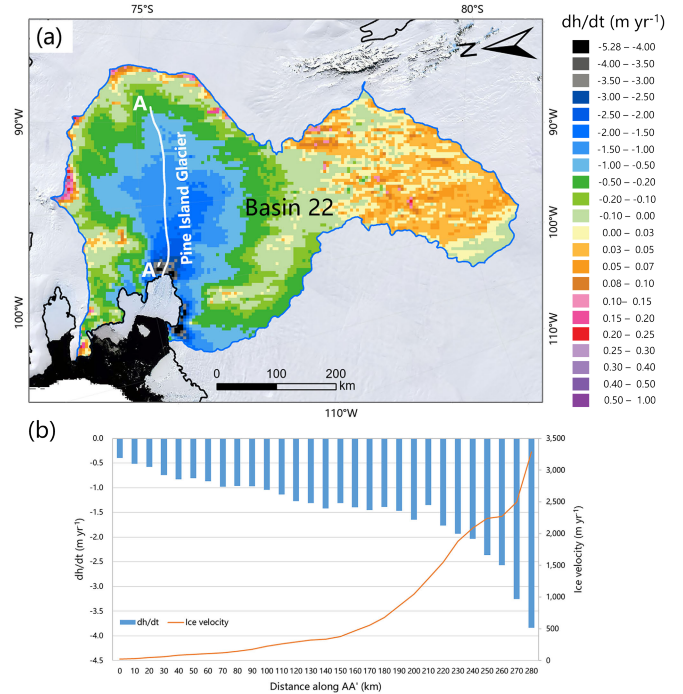


Fig. 8. (a) Estimated ICESat-2 surface elevation change rates in Basin 22 and PIG. Grid spacing is 5 km. Profile AA' illustrates the main trunk of PIG. Blue line indicates the basin boundary [24]. Black line illustrates the grounding line [50]. Background is the Landsat image mosaic of Antarctica (LIMA) [51]. (b) Thinning rate and velocity along the main trunk AA' of PIG.

increasing thinning trend along the main trunk of PIG [AA' in Fig. 8(b)], with an average thinning rate of $\sim -1.433 \text{ m yr}^{-1}$. Thinning at the glacier outlet reaches the highest rate of $\sim -3.794 \text{ m yr}^{-1}$, which is within the long-term range from ~ -3 to $\sim -6 \text{ m yr}^{-1}$ during 1992–2017 observed by multisatellites of ERA, ENVISAT, ICESat, and CryoSat-2 [26], [52], [58].

A direct comparison is performed against a multiyear airborne mission dataset, ATM surface elevation data [59], acquired by an airborne laser altimeter in this region during 2016–2018 (see Fig. 9). The surface elevations measured along the flight routes have an accuracy of 10 cm as assessed by using crossovers at flight intersections [60]. The data are used to produce surface elevation change rates along the flight routes. We calculate the differences of elevation change rates between the two datasets (ICESat-2 minus ATM). The average difference along all flight routes shows an increase of change rates by $-0.28 \pm 0.047 \text{ m yr}^{-1}$, with the maximum of $-0.657 \pm 0.053 \text{ m yr}^{-1}$ occurring in the area before the glacier outlet (Box 1 in Fig. 9), indicating an accelerated thinning close to grounding zone from 2016–2018 to 2019–2023.

We select two relatively stable areas with very low ice flow velocity, less than ~ 6 and $\sim 18 \text{ m yr}^{-1}$ [50] in Boxes 2 and 3 in Fig. 9, respectively, to estimate the ICESat-2 change rate accuracy. The calculated ICESat-2–ATM elevation change rate difference is 2.5 ± 7.4 and $-0.4 \pm 4.5 \text{ cm yr}^{-1}$, respectively, in the two boxes. This result shows a high level of consistency between the two datasets in these two areas from 2016–2018 to 2019–2023.

We further compare our elevation change rates in Basin 22 from ICESat-2 during 2019–2023 [see Fig. 8(a)] with that

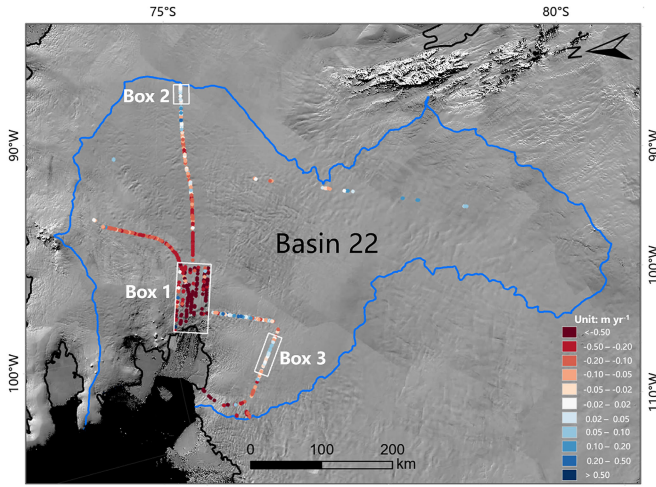


Fig. 9. Validation of ICESat-2 surface elevation change rates using airborne ATM laser altimeter data during 2016–2018 in Basin 22. Box 1 shows a thinning area close to grounding zone. Boxes 2 and 3 are two relatively stable areas with very low ice flow velocity. Blue line indicates the basin boundary [24]. Black line illustrates the grounding line [50]. Background is the Landsat image mosaic of Antarctica (LIMA) [51].

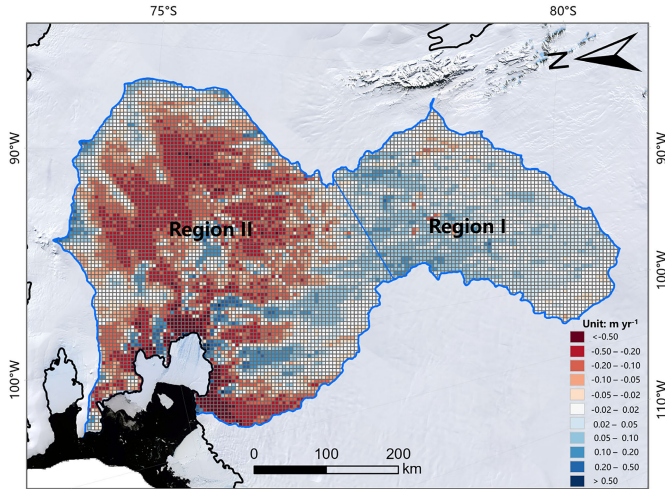


Fig. 10. Comparison of the MECEM results during 2019–2023 with that from ICESat and ICESat-2 during 2003–2019 [23] in Basin 22. The difference map is produced by 2019–2023 – 2003–2019. Blue line indicates the basin boundary [24]. Black line illustrates the grounding line [50]. Background is the Landsat image mosaic of Antarctica (LIMA) [51].

from ICESat and ICESat-2 during 2003–2019 [23], which used the ICESat data from 2003–2009 and the first two cycles of ICESat-2 data from October 2018 to February 2019. Both datasets are not corrected for FAC, elastic and GIA [23], and are gridded at the same spacing of 5 km. A difference map (2019–2023 – 2003–2019) is produced to facilitate the comparison (see Fig. 10).

Overall, both results show glacier volumetric losses in the basin, $-81.9 \pm 0.8 \text{ km}^3 \text{ yr}^{-1}$ during 2019–2023 from the proposed MECEM model and $-67.4 \pm 0.6 \text{ km}^3 \text{ yr}^{-1}$ during 2003–2019 from [23], with an increase of $-14.5 \pm 1 \text{ km}^3 \text{ yr}^{-1}$. This corresponds to a glacier-wide accelerated thinning of $-0.073 \pm 0.025 \text{ m yr}^{-1}$ between the two periods (see Fig. 10). In detail, the southern high inland Region I experienced a slight increase of $0.032 \pm 0.002 \text{ m yr}^{-1}$ in

thickening, while in Region II, the northern branch of the basin, an accelerated thinning at $-0.12 \pm 0.035 \text{ m yr}^{-1}$ occurred. The most significant thinning increase by $-0.781 \pm 0.333 \text{ m yr}^{-1}$ is found along the grounding line. The accelerated thinning in Region II and along grounding line is in line with the findings of speed up during 2007–2022 of the northern branch of the PIG drainage basin [61] and long-term thinning during 2003–2021 in PIG using multisatellite observations [62]. Thickening in Region I may be partly attributed to regional surface mass balance anomalies, such as the extraordinary precipitation event in WAIS during the austral winter of 2019 [63].

V. CONCLUSION

We demonstrate that the proposed MECEM model can fully utilize the unprecedentedly high point density and improved temporal coverage of the photon-counting ICESat-2 satellite altimetric observations. The developed model is applied to produce basin-wide elevation change rates during 2019–2023 in AIS at a grid spacing of 5 km. The modeling results are validated by using GNSS in situ observations, snow stakes measurements, and airborne altimetric survey data. They are also compared with elevation change rates estimated using other satellite altimetry mission observations, such as the ESA multimission radar altimetric dataset and combined ICESat and ICESat-2 data, to quantify the elevation change trends in AIS. We draw the following conclusions.

- 1) The new MECEM model is proven to be effective in the estimation of elevation change rates from ICESat-2 data in basin-wide experimental sites with different spatiotemporal characteristics across Antarctica. The ICESat-2 elevation change rate accuracy reached $1.0 \pm 0.5 \text{ cm yr}^{-1}$ when validated with GNSS in situ measurements at Vostok Station and $2.5 \pm 7.4 \text{ cm yr}^{-1}$ when compared with airborne altimetric measurements in the PIG.
- 2) We separate the periodical precipitation terms from topographic terms to eliminate their correlations through an effective spatiotemporal iterative procedure and demonstrate that the model is capable of estimating the elevation changes as small as $1.8 \pm 0.1 \text{ cm yr}^{-1}$ in the Vostok subglacial lake region.
- 3) The MECEM modeling results show an increase of $0.103 \pm 0.001 \text{ m yr}^{-1}$ in thickening from 2017–2021 to 2019–2023 in a drainage basin in Dronning Maud Land and an accelerated thinning by $-0.12 \pm 0.035 \text{ m yr}^{-1}$ from 2003–2019 to 2019–2023 in the northern part of the fast-flowing PIG region.

The developed MECEM model can be applied to estimate volumetric and mass changes of the entire AIS and its associated contribution to the GSLR.

APPENDICES

A. Crossover Analysis

At a crossover, if the elapsed time between the two intersecting tracks is small relative to the natural rate of the elevation change, the elevation difference can be used to assess the

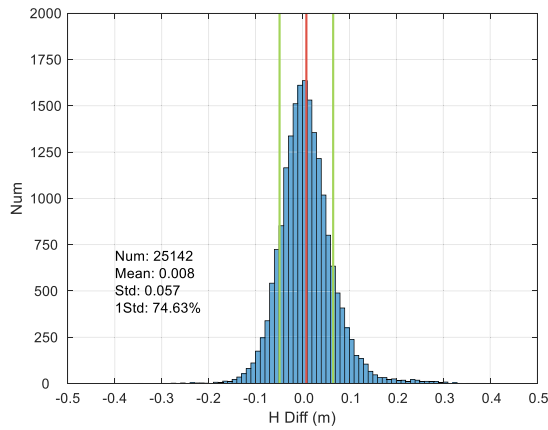


Fig. 11. Histogram of elevation differences at crossovers in the Vostok region from Cycle 1 to Cycle 7.

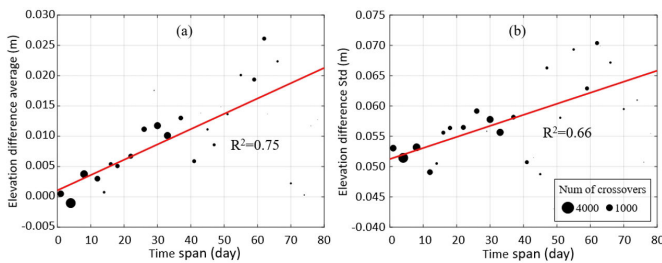


Fig. 12. Crossovers with relatively short time spans in the Vostok region show smaller elevation differences and standard deviations. There is a linear correlation (a) between time span and elevation difference and (b) between time span and standard deviation.

elevation measurement precision [9], [54]. Here, we analyze crossovers computed from the ICESat-2 ATL06 data (Cycles 1–7, after filtering out of low-quality points flagged with “0”) by using an intersection function in Antarctic mapping tools for MATLAB [39]. Each crossover center is determined by a linear intersection using elevation points along the ascending and descending tracks within a neighborhood of 40 m.

Within a cycle, in the Vostok region, there are in average ~ 3600 crossovers or a point density of one crossover per 2 km cell (2 km 2 km). The time span between the crossover tracks ranges from 0.5 days to 77.4 days. With repeated measurements of seven cycles, there are a total of 25142 crossover observations that resulted in an average elevation difference of 0.8 cm and a standard deviation of 5.7 cm in this lake region (see Fig. 11).

Furthermore, the crossovers with short time spans of less than 45 days ($\sim 77\%$) have elevation differences smaller than 1.5 cm and standard deviations of less than 6 cm (see Fig. 12), indicating an R^2 correlation of 0.75 and 0.66, respectively. Therefore, if the elevation differences at crossovers are measured within a relatively short time span, they are less affected by long-term changes.

In AIS, we examine crossovers with a grid of 30-km spacing (see Fig. 13). Those crossovers with elevation differences greater than 5 m are treated as outliers and are not considered. We establish a distribution of elevation differences of the AIS grid, which are calculated as the averages of crossovers within the grid cells. For example, in the vast inland region

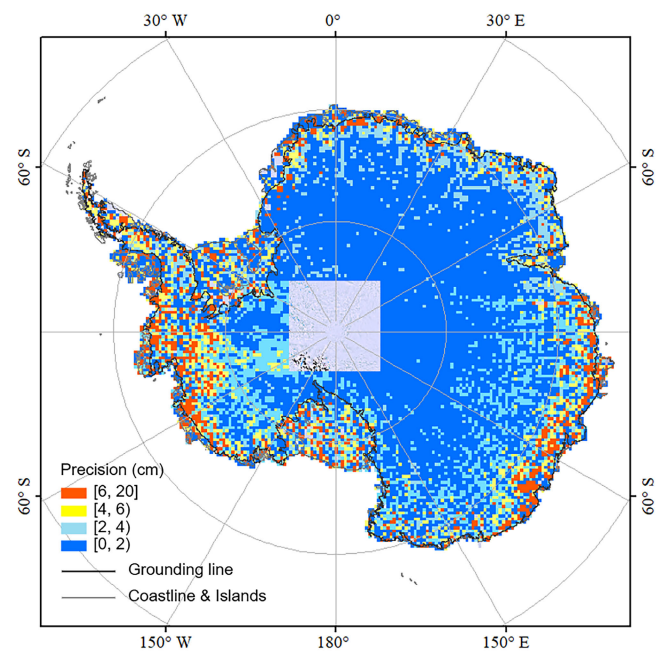


Fig. 13. Based on ICESat-2 ATL 06 data from Cycle 1 to Cycle 7, elevation differences in AIS are calculated as a grid of a 30-km spacing averaged from crossovers.

of East Antarctica (see Fig. 13), the elevation differences are in average 2 cm or less. However, in lower latitude coastal regions, elevation differences are 2–8 cm. Large differences occur in the Amundsen Sea sector and Wilkes Land region, where fast changes, such as acceleration and ice sheet thinning, are reported [2], [5], [23]. Thus, the precision of ICESat-2 ATL06 crossovers is very high, $\sim 87\%$ of which have their average elevation differences smaller than 4 cm or less.

B. Precipitation Effect Analysis

We perform an analysis of the effect of periodical changes, such as precipitation, on the elevation within a limited area (e.g., diamond unit) in three different regions in AIS. Within a diamond unit in the Vostok region, we name four corners as Corner 1 to Corner 4, each of which consists of four crossovers [see Fig. 14(a)]. Since the lake surface is relatively flat, crossover intersection locations are determined accurately. Thus, when we make a difference between two elevation observation equations at a crossover, the topographic terms are canceled out and only the elevation change rate term and precipitation terms remain (2). Using elevation observations at four crossovers of a diamond unit corner over all cycles, we are able to estimate the elevation change rate and a set of parameters (amplitudes and phases) of the precipitation terms for the corner. We use these periodical precipitation parameters to plot curves corresponding to four corners of the diamond unit [see Fig. 14(b)]. It is shown that these reconstructed periodical curves by the MECEM model exhibit a consistent precipitation pattern, with an RMSE of 3 cm between the curves. That means that a fixed annual phase and a varying phase with varying amplitudes are sufficient to model the precipitation effect within a diamond unit.

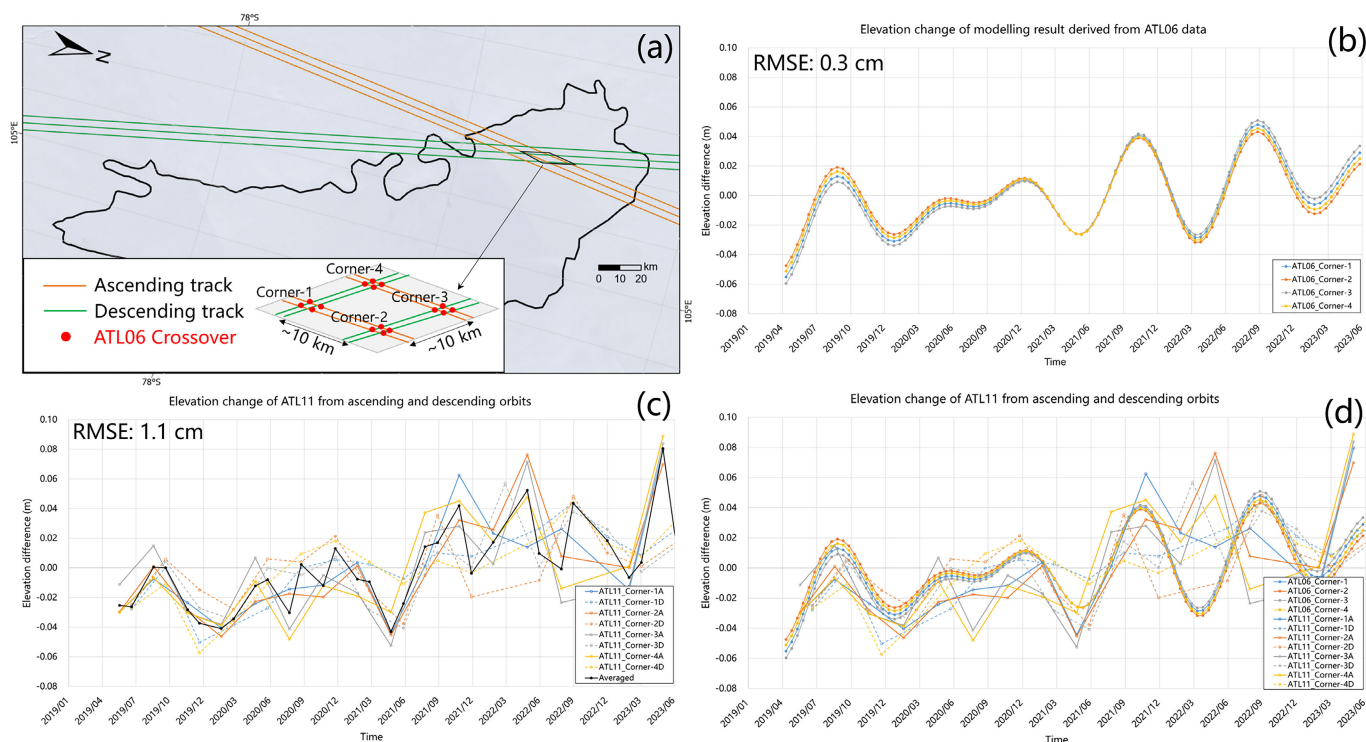
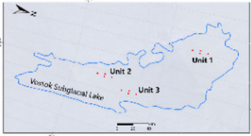

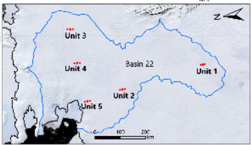


Fig. 14. Effect of periodical changes, such as precipitation, on the elevation within a diamond unit. (a) Diamond unit formed by ascending and descending tracks (black diamond) and crossovers (red dots in inset) at four corners, (b) MECEM periodical curves of the four corners, (c) ATL11 elevation time series of the crossovers at four corners, and (d) consistent precipitation pattern shown by the MECEM curves and ATL11 elevation time series.

TABLE II
11 HOMOGENEITY OF PRECIPITATION PATTERN WITHIN A DIAMOND UNIT IN DIFFERENT REGIONS IN AIS

Basin	Diamond Unit ID in Basin	$\frac{dh}{dt}$ (m yr ⁻¹)	RMSE of MECEM curve (m)	RMSE of ATL11 time series (m)	Diamond Unit location in Basin
Vostok	1	0.015	0.003	0.011	
	2	0.012	0.007	0.013	
	3	0.016	0.003	0.014	
Basin 5	1	0.017	0.002	0.015	
	2	0.003	0.016	0.025	
	3	0.412	0.084	0.106	
Basin 22	1	0.046	0.013	0.015	
	2	-0.005	0.018	0.040	
	3	-0.389	0.063	0.100	
	4	-1.353	0.023	0.049	
	5	-1.476	0.133	0.319	

For comparison, we further use the ATL11 ice surface elevation product data (<https://doi.org/10.5067/ATLAS/ATL11.005>, last access: October 25, 2023) to compute the corresponding

elevation time series at the four corners, which are solid lines (ascending tracks) and dashed lines (descending tracks) in Fig. 14(c). Despite of their larger dispersion (RMSE of

TABLE III
AUXILIARY DATA USED IN THIS STUDY

Region	Data set	Timespan	Accuracy	Source
Vostok	Surface elevation change rates from kinematic GNSS observations	2001–2013	$\pm 0.005 \text{ m yr}^{-1}$	Richter et al., 2014 [25]
Basin 5	Surface elevation change rates from ESA multi-mission radar altimetric dataset	2017–2021	Basin 5: $\pm 0.52 \text{ m yr}^{-1}$ Region I: $\pm 0.065 \text{ m yr}^{-1}$	Shepherd et al., 2019 [52]
Basin 11	Ice flux across AA' calculated based on GNSS-derived ice velocity	1997–2009	0.9 Gt yr^{-1}	Cui et al., 2020 [29]
	In situ snow stake measurements	2019–2023	—	Will provide upon request
Basin 22	Surface elevation measurements from IceBridge ATM	2016–2018	0.100 m or better	Studinger, 2014 [59]
	Elevation change rates from ICESat and ICESat-2	2003–2019	$\pm 0.024 \text{ m yr}^{-1}$	Smith et al., 2020 [23]

1.1 cm), the ATL11 elevation time series also shows a similar precipitation pattern as that from the MECEM model within the diamond unit [see Fig. 14(d)].

Hence, we select a total of 11 diamond units to further examine homogeneity of the precipitation effect within a diamond unit in different regions of AIS, 3 in Vostok, 3 in Basin 5 and 5 in Basin 22. The MECEM results show that the periodical terms are able to model the precipitation effect on the elevation within diamond units with RMSEs at a mm to cm level in Vostok and Basin 5, where elevation change rates are relatively small (see Table II). In Basin 22, the RMSEs are at a cm level, except $\sim 13 \text{ cm}$ at Unit 5 that is close to grounding line of PIG and has a large elevation change rate of $\sim -1.476 \text{ m yr}^{-1}$.

In summary, the MECEM model and ATL11 product use the same ATL06 data, but they process data using their own independent models. Both show that the precipitation effect on elevation within a diamond unit has a similar pattern and, thus, can be modeled by using one set of parameters.

C. Uncertainty Estimation

Uncertainties of the estimated parameters, such the topographic polynomial coefficients $(a_0, a_1, a_2, \dots, a_9)$ and elevation change rate (dh/dt) , are given as internal error indicators that are computed through error propagation law [44]. For example, in implementation, Equation 3 can be written as an observation equation in a matrix form

$$z = Ax + \delta$$

where z is a vector of everything on the left-hand side of the equal sign in (3). It is populated for all elevation measurements within a window of computation. x is the unknown vector containing (dh/dt) and $(a_0, a_1, a_2, \dots, a_9)$. A is the design matrix filled by coefficients before x in (3). δ is the residual vector.

Given uncertainties of all elevation measurements within the window from the ICESat-2 product, we build a diagonal weight matrix C , assuming that the measurements are uncorrelated. Consequently, the covariance matrix of x is expressed as

$$P = (A^T C^{-1} A)^{-1}.$$

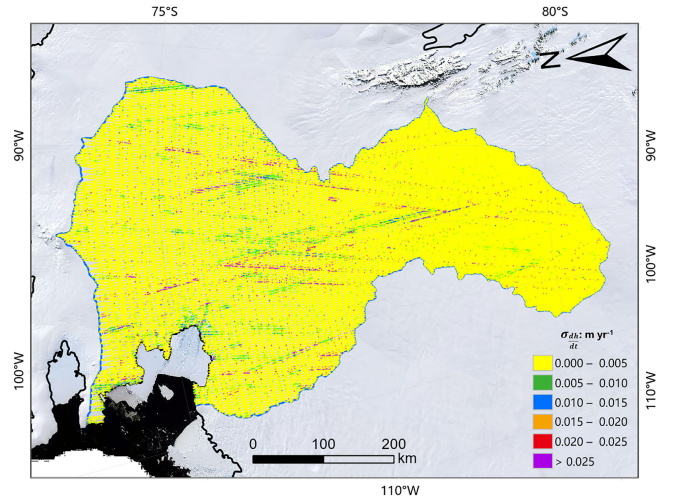


Fig. 15. Uncertainty distribution of (dh/dt) in Basin 22.

Variances of the unknowns are expressed as $\sigma_o^2 p_{ij}$, with σ_o^2 being the unit weight variance and p_{ij} as the diagonal elements of matrix P [44]. We use square root values as their uncertainties.

Specifically, we use the “h_i_sigma” flag in ATL06 data to compute the weights of the elevation measurements in the above equation, which consider the influences of differences between the strong and weak beams, including the first-photon bias (FPB) and number of photons per pulse [34].

Using Basin 22 containing the fast-changing PIG as an example, Fig. 15 illustrates the uncertainty distribution of (dh/dt) , which are mostly under 0.5 cm yr^{-1} . Fig. 16 shows the uncertainties of $(a_0, a_1, a_2, \dots, a_9)$.

Similarly, uncertainties of the unknowns in (4) can be computed in the same way using the above equations.

Finally, using the root mean square error (RMSE) of all residual elements in δ , we can estimate the elevation uncertainty, which also indicates the performance of the model (see Fig. 17). Since horizontal geolocation errors are not considered in (3), the elevation uncertainty may be larger [64].

D. Auxiliary Data

See Table III.

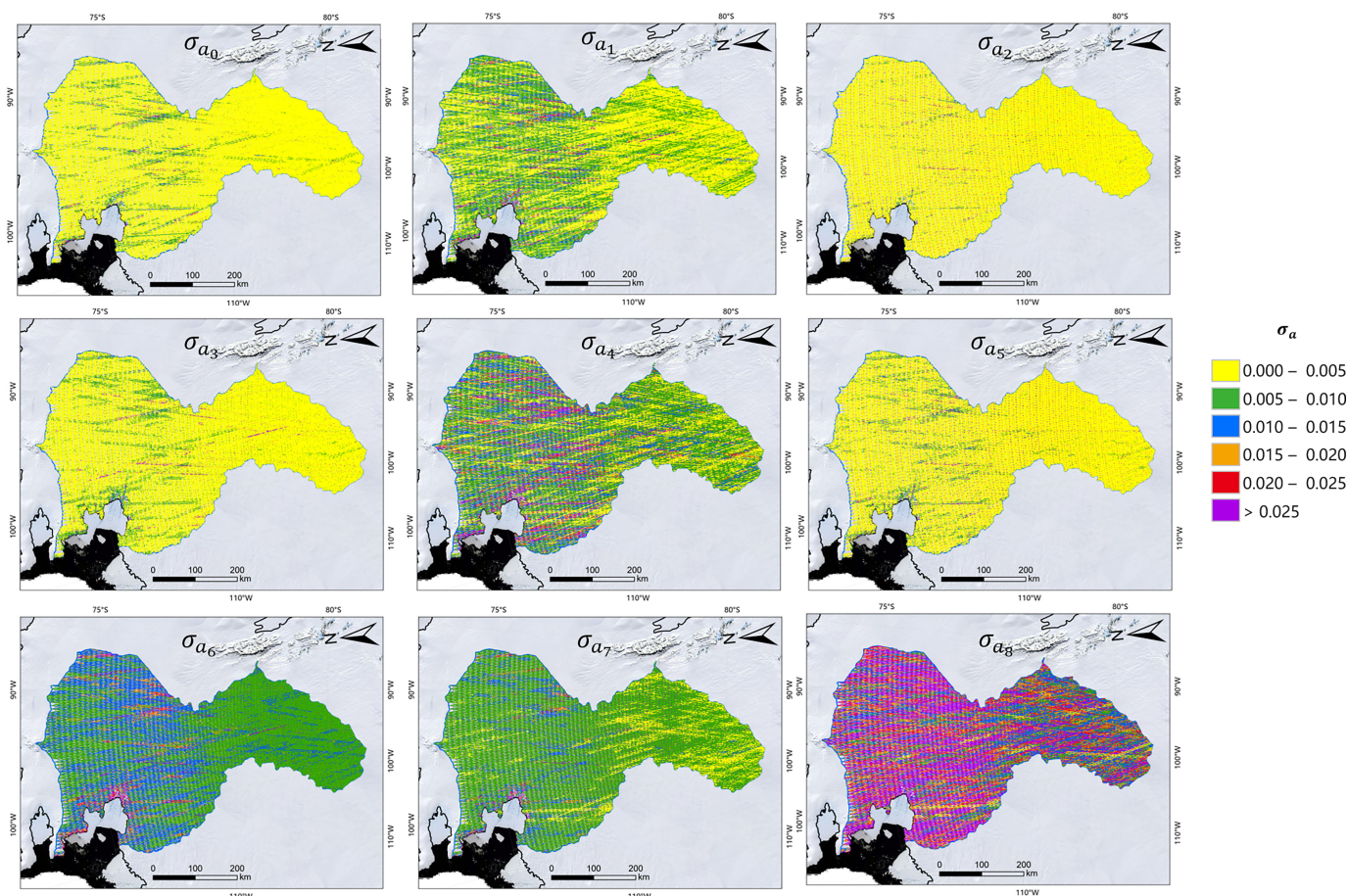


Fig. 16. Uncertainty distribution of ($a_0, a_1, a_2, \dots, a_9$) in Basin 22.

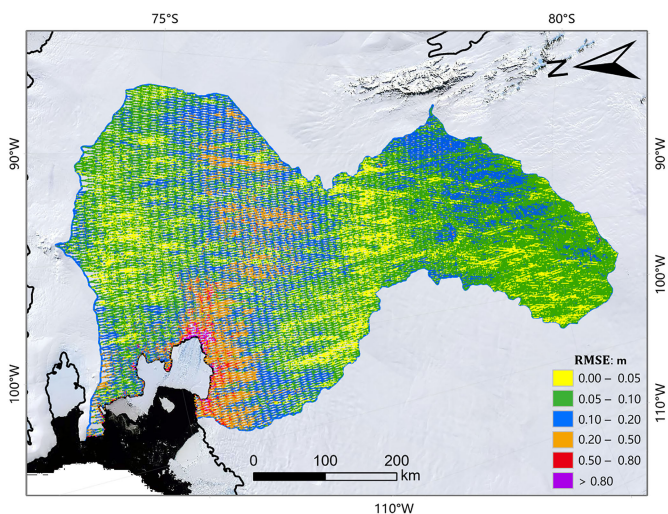


Fig. 17. RMSE of elevation measurements in Basin 22.

ACKNOWLEDGMENT

The authors appreciate support from Fundamental Research Funds for the Central Universities.

REFERENCES

[1] A. Shepherd et al., “Mass balance of the Antarctic ice sheet from 1992 to 2017,” *Nature*, vol. 558, no. 7709, pp. 219–222, 2018, doi: 10.1038/s41586-018-0179-y.

[2] E. Rignot, J. Mouginot, B. Scheuchl, M. van den Broeke, M. J. van Wessem, and M. Morlighem, “Four decades of Antarctic ice sheet mass balance from 1979–2017,” *Proc. Nat. Acad. Sci. USA*, vol. 116, no. 4, pp. 1095–1103, Jan. 2019, doi: 10.1073/pnas.1812883116.

[3] B. Bronselaer et al., “Change in future climate due to Antarctic meltwater,” *Nature*, vol. 564, no. 7734, pp. 53–58, Dec. 2018, doi: 10.1038/s41586-018-0712-z.

[4] I. N. Otosaka et al., “Mass balance of the Greenland and Antarctic ice sheets from 1992 to 2020,” *Earth Syst. Sci. Data*, vol. 15, no. 4, pp. 1597–1616, Apr. 2023, doi: 10.5194/essd-15-1597-2023.

[5] A. S. Gardner et al., “Increased West Antarctic and unchanged east Antarctic ice discharge over the last 7 years,” *Cryosphere*, vol. 12, no. 2, pp. 521–547, Feb. 2018, doi: 10.5194/tc-12-521-2018.

[6] Q. Shen et al., “Recent high-resolution Antarctic ice velocity maps reveal increased mass loss in Wilkes Land, East Antarctica,” *Sci. Rep.*, vol. 8, no. 1, p. 4477, 2018, doi: 10.1038/s41598-018-22765-0.

[7] R. Li et al., “Satellite record reveals 1960s acceleration of Totten Ice Shelf in East Antarctica,” *Nature Commun.*, vol. 14, no. 1, p. 4061, 2023, doi: 10.1038/s41467-023-39588-x.

[8] Y. Tian et al., “On the conversion of Antarctic ice-mass change to sea level equivalent,” *Mar. Geodesy*, vol. 38, no. 1, pp. 89–97, 2015, doi: 10.1080/01490419.2014.969458.

[9] C. A. Shuman et al., “ICESat Antarctic elevation data: Preliminary precision and accuracy assessment,” *Geophys. Res. Lett.*, vol. 33, no. 7, pp. 1–4, 2006, doi: 10.1029/2005GL025227.

[10] A. C. Brenner, J. P. DiMarzio, and H. J. Zwally, “Precision and accuracy of satellite radar and laser altimeter data over the continental ice sheets,” *IEEE Trans. Geosci. Remote Sens.*, vol. 45, no. 2, pp. 321–331, Feb. 2007, doi: 10.1109/TGRS.2006.887172.

[11] H. J. Zwally et al., “Mass gains of the Antarctic ice sheet exceed losses,” *J. Glaciol.*, vol. 61, no. 230, pp. 1019–1036, 2015, doi: 10.3189/2015JoG15J071.

- [12] T. Scambos and C. Shuman, "Comment on 'Mass gains of the Antarctic ice sheet exceed losses' by H.J. Zwally and others," *J. Glaciol.*, vol. 62, no. 233, pp. 599–603, 2016, doi: [10.1017/jog.2016.59](https://doi.org/10.1017/jog.2016.59).
- [13] A. Richter, M. Horwath, and R. Dietrich, "Comment on Zwally and others (2015)-Mass gains of the Antarctic ice sheet exceed losses," *J. Glaciol.*, vol. 62, no. 233, pp. 604–606, 2016, doi: [10.1017/jog.2016.60](https://doi.org/10.1017/jog.2016.60).
- [14] H. J. Zwally et al., "Greenland ice sheet mass balance: Distribution of increased mass loss with climate warming; 2003–07 versus 1992–2002," *J. Glaciol.*, vol. 57, no. 201, pp. 88–102, 2011, doi: [10.3189/0022143111795306682](https://doi.org/10.3189/0022143111795306682).
- [15] B. M. Csatho et al., "Laser altimetry reveals complex pattern of Greenland ice sheet dynamics," *Proc. Nat. Acad. Sci. USA*, vol. 111, no. 52, pp. 18478–18483, 2014, doi: [10.1073/pnas.1411680112](https://doi.org/10.1073/pnas.1411680112).
- [16] A. Groh et al., "Evaluating GRACE mass change time series for the Antarctic and Greenland ice sheet—Methods and results," *Geosciences*, vol. 9, no. 10, p. 415, Sep. 2019, doi: [10.3390/geosciences9100415](https://doi.org/10.3390/geosciences9100415).
- [17] L. S. Sørensen et al., "Mass balance of the Greenland ice sheet (2003–2008) from ICESat data—The impact of interpolation, sampling and firm density," *Cryosphere*, vol. 5, no. 1, pp. 173–186, 2011, doi: [10.5194/tc-5-173-2011](https://doi.org/10.5194/tc-5-173-2011).
- [18] H. Ewert, A. Groh, and R. Dietrich, "Volume and mass changes of the Greenland ice sheet inferred from ICESat and GRACE," *J. Geodyn.*, vols. 59–60, pp. 111–123, Sep. 2012, doi: [10.1016/j.jog.2011.06.003](https://doi.org/10.1016/j.jog.2011.06.003).
- [19] B. E. Smith, C. R. Bentley, and C. F. Raymond, "Recent elevation changes on the ice streams and ridges of the Ross Embayment from ICESat crossovers," *Geophys. Res. Lett.*, vol. 32, no. 21, pp. 1–5, 2005, doi: [10.1029/2005GL024365](https://doi.org/10.1029/2005GL024365).
- [20] D. Felikson et al., "Comparison of elevation change detection methods from ICESat altimetry over the Greenland ice sheet," *IEEE Trans. Geosci. Remote Sens.*, vol. 55, no. 10, pp. 5494–5505, Oct. 2017, doi: [10.1109/TGRS.2017.2709303](https://doi.org/10.1109/TGRS.2017.2709303).
- [21] H. Xie et al., "A comparative study of changes in the Lambert Glacier/Amery Ice Shelf system, East Antarctica, during 2004–2008 using gravity and surface elevation observations," *J. Glaciol.*, vol. 62, no. 235, pp. 888–904, 2016, doi: [10.1017/jog.2016.76](https://doi.org/10.1017/jog.2016.76).
- [22] T. Schenk and B. Csatho, "A new methodology for detecting ice sheet surface elevation changes from laser altimetry data," *IEEE Trans. Geosci. Remote Sens.*, vol. 50, no. 9, pp. 3302–3316, Sep. 2012, doi: [10.1109/TGRS.2011.2182357](https://doi.org/10.1109/TGRS.2011.2182357).
- [23] B. Smith et al., "Pervasive ice sheet mass loss reflects competing ocean and atmosphere processes," *Science*, vol. 368, no. 6496, pp. 1239–1242, Jun. 2020, doi: [10.1126/science.aaz5845](https://doi.org/10.1126/science.aaz5845).
- [24] H. J. Zwally et al., "Antarctic and Greenland drainage systems," GSFC Cryospheric Sci. Lab., Greenbelt, MD, USA, 2012. [Online]. Available: http://icesat4.gsfc.nasa.gov/cryo_data/ant_grn_drainage_systems.php
- [25] A. Richter et al., "Height changes over subglacial Lake Vostok, East Antarctica: Insights from GNSS observations," *J. Geophys. Res., Earth Surf.*, vol. 119, no. 11, pp. 2460–2480, Nov. 2014, doi: [10.1002/2014JF003228](https://doi.org/10.1002/2014JF003228).
- [26] L. Schröder et al., "Four decades of Antarctic surface elevation changes from multi-mission satellite altimetry," *Cryosphere*, vol. 13, no. 2, pp. 427–449, 2019, doi: [10.5194/tc-13-427-2019](https://doi.org/10.5194/tc-13-427-2019).
- [27] V. Goel, J. Brown, and K. Matsuoka, "Glaciological settings and recent mass balance of Blåskimen Island in Dronning Maud Land, Antarctica," *Cryosphere*, vol. 11, no. 6, pp. 2883–2896, 2017, doi: [10.5194/tc-11-2883-2017](https://doi.org/10.5194/tc-11-2883-2017).
- [28] T. Feng et al., "A hierarchical network densification approach for reconstruction of historical ice velocity fields in East Antarctica," *J. Glaciol.*, vol. 69, no. 274, pp. 281–300, 2023, doi: [10.1017/jog.2022.58](https://doi.org/10.1017/jog.2022.58).
- [29] X. Cui et al., "The ice flux to the Lambert Glacier and Amery ice shelf along the Chinese inland traverse and implications for mass balance of the drainage basins, East Antarctica," *Polar Res.*, vol. 39, pp. 1–10, Nov. 2020, doi: [10.33265/polar.v39.3582](https://doi.org/10.33265/polar.v39.3582).
- [30] R. Li et al., "Assessment of ICESat-2 ice surface elevations over the Chinese Antarctic research expedition (CHINARE) route, East Antarctica, based on coordinated multi-sensor observations," *Cryosphere*, vol. 15, no. 7, pp. 3083–3099, 2021, doi: [10.5194/tc-15-3083-2021](https://doi.org/10.5194/tc-15-3083-2021).
- [31] T. Markus et al., "The ice, cloud, and land elevation Satellite-2 (ICESat-2): Science requirements, concept, and implementation," *Remote Sens. Environ.*, vol. 190, pp. 260–273, Mar. 2017, doi: [10.1016/j.rse.2016.12.029](https://doi.org/10.1016/j.rse.2016.12.029).
- [32] T. A. Neumann et al., "The Ice, cloud, and land elevation Satellite-2 mission: A global geolocated photon product derived from the advanced topographic laser altimeter system," *Remote Sens. Environ.*, vol. 233, Nov. 2019, Art. no. 111325, doi: [10.1016/j.rse.2019.111325](https://doi.org/10.1016/j.rse.2019.111325).
- [33] L. A. Magruder, K. M. Brunt, and M. Alonzo, "Early ICESat-2 on-orbit geolocation validation using ground-based corner cube retro-reflectors," *Remote Sens.*, vol. 12, no. 21, p. 3653, Nov. 2020, doi: [10.3390/rs12213653](https://doi.org/10.3390/rs12213653).
- [34] B. Smith et al., "Land ice height-retrieval algorithm for NASA's ICESat-2 photon-counting laser altimeter," *Remote Sens. Environ.*, vol. 233, Nov. 2019, Art. no. 111352, doi: [10.1016/j.rse.2019.111352](https://doi.org/10.1016/j.rse.2019.111352).
- [35] K. M. Brunt, T. A. Neumann, and B. E. Smith, "Assessment of ICESat-2 ice sheet surface heights, based on comparisons over the interior of the Antarctic ice sheet," *Geophys. Res. Lett.*, vol. 46, no. 22, pp. 13072–13078, Nov. 2019, doi: [10.1029/2019GL084886](https://doi.org/10.1029/2019GL084886).
- [36] K. M. Brunt et al., "Comparisons of satellite and airborne altimetry with ground-based data from the interior of the Antarctic ice sheet," *Geophys. Res. Lett.*, vol. 48, no. 2, pp. 1–9, 2021, doi: [10.1029/2020GL090572](https://doi.org/10.1029/2020GL090572).
- [37] Smith et al., "Algorithm theoretical basis document (ATBD) for land-ice DEM (ATL14) and land-ice height change (ATL15)," Goddard Space Flight Center, Greenbelt, MD, USA, Tech. Rep., Version 3, Sep. 2023, pp. 5–6. [Online]. Available: https://nsidc.org/sites/default/files/documents/technical-reference/icesat2_atl14_atl15_atbd_v003.pdf
- [38] B. Smith et al., "Ice, cloud, and land elevation Satellite-2 (ICESat-2) project algorithm theoretical basis document (ATBD) for land-ice along-track products part 2: Slope-corrected land ice height time series (ATL11), version 6," Goddard Space Flight Center, Greenbelt, MD, USA, Tech. Rep., Version 6, Jun. 2023, p. 5. [Online]. Available: https://nsidc.org/sites/default/files/documents/technical-reference/icesat2_atl11_atbd_v006.pdf
- [39] C. A. Greene, D. E. Gwyther, and D. D. Blankenship, "Antarctic mapping tools for MATLAB," *Comput. Geosci.*, vol. 104, pp. 151–157, Jul. 2017, doi: [10.1016/j.cageo.2016.08.003](https://doi.org/10.1016/j.cageo.2016.08.003).
- [40] J. H. Wen et al., "Mass budgets of the Lambert, Mellor and Fisher Glaciers and basal fluxes beneath their flowbands on Amery ice shelf," *Sci. China D, Earth Sci.*, vol. 50, no. 11, pp. 1693–1706, 2007, doi: [10.1007/s11430-007-0120-y](https://doi.org/10.1007/s11430-007-0120-y).
- [41] Z. Gu et al., "Experimental results of elevation change analysis in the Antarctic ice sheet using DEMs from ERS and ICESat data," *Ann. Glaciol.*, vol. 55, no. 66, pp. 198–204, 2014, doi: [10.3189/2014AoG66A124](https://doi.org/10.3189/2014AoG66A124).
- [42] P. Fretwell et al., "Bedmap2: Improved ice bed, surface and thickness datasets for Antarctica," *Cryosphere*, vol. 7, no. 1, pp. 375–393, 2013, doi: [10.5194/tc-7-375-2013](https://doi.org/10.5194/tc-7-375-2013).
- [43] J. P. Snyder, "Lambert azimuthal equal-area projection," in *Map Projections—A Working Manual*, vol. 1395. Washington, DC, USA: U.S. Government Printing Office, 1987, pp. 182–187.
- [44] C. D. Ghilani and P. R. Wolf, *Adjustment Computations: Spatial Data Analysis*, 4th ed. Hoboken, NJ, USA: Wiley, 2006, pp. 173–232.
- [45] P. C. Hansen, V. Pereyra, and G. Scherer, *Least Squares Data Fitting With Applications*. Baltimore, MD, USA: Johns Hopkins Univ. Press, 2013, pp. 163–185.
- [46] X. Li et al., "Ice flow dynamics and mass loss of Totten Glacier, East Antarctica, from 1989 to 2015," *Geophys. Res. Lett.*, vol. 43, no. 12, pp. 6366–6373, 2016, doi: [10.1002/2016GL069173](https://doi.org/10.1002/2016GL069173).
- [47] O. Troshichev et al., "IMF-associated cloudiness above near-pole station Vostok: Impact on wind regime in winter Antarctica," *J. Atmos. Sol-Terr. Phys.*, vol. 70, no. 10, pp. 1289–1300, 2008, doi: [10.1016/j.jastp.2008.04.003](https://doi.org/10.1016/j.jastp.2008.04.003).
- [48] S. V. Popov and Y. B. Chernoglazov, "Vostok Subglacial Lake, East Antarctica: Lake shoreline and subglacial water caves," *Ice Snow*, vol. 1, no. 113, pp. 12–24, 2011.
- [49] I. Velicogna et al., "Continuity of ice sheet mass loss in Greenland and Antarctica from the GRACE and GRACE follow-on missions," *Geophys. Res. Lett.*, vol. 47, no. 8, pp. 1–8, 2020, doi: [10.1029/2020GL087291](https://doi.org/10.1029/2020GL087291).
- [50] E. Rignot, J. Mouginot, and B. Scheuchl, "Ice flow of the Antarctic ice sheet," *Science*, vol. 333, no. 6048, pp. 1427–1430, 2011, doi: [10.1126/science.1208336](https://doi.org/10.1126/science.1208336).
- [51] R. Bindshadler et al., "The Landsat image mosaic of Antarctica," *Remote Sens. Environ.*, vol. 112, no. 12, pp. 4214–4226, Dec. 2008, doi: [10.1016/j.rse.2008.07.006](https://doi.org/10.1016/j.rse.2008.07.006).
- [52] A. Shepherd et al., "Trends in Antarctic ice sheet elevation and mass," *Geophys. Res. Lett.*, vol. 46, no. 14, pp. 8174–8183, 2019, doi: [10.1029/2019GL082182](https://doi.org/10.1029/2019GL082182).
- [53] M. McMillan et al., "Increased ice losses from Antarctica detected by CryoSat-2," *Geophys. Res. Lett.*, vol. 41, no. 11, pp. 3899–3905, 2014, doi: [10.1002/2014GL060111](https://doi.org/10.1002/2014GL060111).

- [54] H. Xie, W. Du, G. Hai, L. Chen, H. Tang, and X. Tong, "Precision and bias comparison between laser and radar altimetry data in the Amundsen sea embayment and the Lambert-Amery system of Antarctica," *IEEE J. Sel. Topics Appl. Earth Observ. Remote Sens.*, vol. 12, no. 11, pp. 4342–4350, Nov. 2019, doi: [10.1109/JSTARS.2019.2947547](https://doi.org/10.1109/JSTARS.2019.2947547).
- [55] T. A. Scambos et al., "Extent of low-accumulation 'wind glaze' areas on the East Antarctic Plateau: Implications for continental ice mass balance," *J. Glaciol.*, vol. 58, no. 210, pp. 633–647, 2012, doi: [10.3189/2012JoG11J232](https://doi.org/10.3189/2012JoG11J232).
- [56] M. Ding et al., "Spatial variability of surface mass balance along a traverse route from Zhongshan station to Dome A, Antarctica," *J. Glaciol.*, vol. 57, no. 204, pp. 658–666, 2011, doi: [10.3189/002214311797409820](https://doi.org/10.3189/002214311797409820).
- [57] H. A. Fricker, R. C. Warner, and I. Allison, "Mass balance of the Lambert Glacier–Amery ice shelf system, East Antarctica: A comparison of computed balance fluxes and measured fluxes," *J. Glaciol.*, vol. 46, no. 155, pp. 561–570, 2000, doi: [10.3189/172756500781832765](https://doi.org/10.3189/172756500781832765).
- [58] H. D. Pritchard et al., "Extensive dynamic thinning on the margins of the Greenland and Antarctic ice sheets," *Nature*, vol. 461, no. 7266, pp. 971–975, 2009, doi: [10.1038/nature08471](https://doi.org/10.1038/nature08471).
- [59] M. Studinger, "IceBridge ATM L2 Icessn elevation, slope, and roughness. Version 2," NASA Nat. Snow Ice Data Center Distrib. Act. Arch. Center, Washington, DC, USA, Tech. Rep., Version 2, 2014, doi: [10.5067/CPRXXK3F39RV](https://doi.org/10.5067/CPRXXK3F39RV).
- [60] N. T. Kurtz et al., "Sea ice thickness, freeboard, and snow depth products from operation IceBridge airborne data," *Cryosphere*, vol. 7, no. 4, pp. 1035–1056, 2013, doi: [10.5194/tc-7-1035-2013](https://doi.org/10.5194/tc-7-1035-2013).
- [61] E. Rignot et al., "Changes in Antarctic ice sheet motion derived from satellite radar interferometry between 1995 and 2022," *Geophys. Res. Lett.*, vol. 49, no. 23, pp. 1–10, 2022, doi: [10.1029/2022GL100141](https://doi.org/10.1029/2022GL100141).
- [62] L. Yue et al., "Reconstructing continuous ice sheet elevation changes in the Amundsen sea sector during 2003–2021 by merging Envisat, ICESat, CryoSat-2, and ICESat-2 multi-altimeter observations," *J. Geophys. Res., Earth Surf.*, vol. 128, no. 5, pp. 1–21, 2023, doi: [10.1029/2022JF007020](https://doi.org/10.1029/2022JF007020).
- [63] S. Adusumilli et al., "Atmospheric river precipitation contributed to rapid increases in surface height of the West Antarctic ice sheet in 2019," *Geophys. Res. Lett.*, vol. 48, no. 5, pp. 1–11, 2021, doi: [10.1029/2020GL091076](https://doi.org/10.1029/2020GL091076).
- [64] T. Hao et al., "Impact of slopes on ICESat-2 elevation accuracy along the CHINARE route in East Antarctica," *IEEE J. Sel. Topics Appl. Earth Observ. Remote Sens.*, vol. 15, pp. 5636–5643, 2022, doi: [10.1109/JSTARS.2022.3189042](https://doi.org/10.1109/JSTARS.2022.3189042).